Modeling Finite Nano Systems

Forrest H. Kaatz, Mesalands Community College, Tucumcari, NM, USA
Adhemar Bultheel, Dept. Computer Sci., KU Leuven, Heverlee, Belgium

Abstract

Modeling the nanoscale can occur by limiting the large-scale nature of arrays and nano systems to a finite size, or by modeling a single nano object. We look at modeling nano systems from a theoretical graph network view, where a graph has atoms at a vertex and links represent bonds. In this way, we can calculate standard statistical mechanics functions (entropy, enthalpy, and free energy) and matrix indices (Wiener Index) of finite nano structures, such as fullerenes, carbon nanotubes, and graphene nanoflakes. The Euclidean Wiener Index (topographical index) is compared with its topological (standard) counterpart. For many of these parameters, the data have power law behavior, especially when plotted versus the number of bonds or the number of atoms. Ideally, the placement of nanosized systems could be fabricated in such a way that the order and location of the objects is as specified. We consider measuring the order in finite nanoporous arrays via the pair distribution function and by reciprocal space parameters. Porous arrays have been made in triangular, hexagonal and square geometries, and we compare the experimental versions with ideal models. An order parameter derived from the pair distribution function takes values from zero to one: whereas, a reciprocal space parameter has nominal values from zero to ten. We conclude with a summary and indications for future work.

Introduction

Nanoscale systems encompass a wide variety of scientific and technological materials, but in general refer to systems from 1 nm to 100 nm in size. We focus on quantifying finite systems, including nanoarrays meant to fabricate nanomaterials, i.e, 0D quantum dots and fullerenes, 1D nanotubes, and finite nanoflakes of 2D graphene. These finite systems lend themselves to numerical calculation from a graph theoretical view, where atoms are located at lattice points and bonds are represented by links in the graph. We calculate standard statistical mechanics functions and matrix indices, such as the Wiener Index [1].

Carbon has many allotropes (diamond, graphite, fullerenes, and carbon nanotubes, (CNTs)) that illustrate the amazing chemical and structural diversity of element number six. We consider the nanosized forms in our calculations; fullerenes, CNTs, and graphene nanoflakes (GNFs). Fullerenes were discovered in 1985 [2], carbon nanotubes in 1991 [3], and graphene in 2004 [4]. As a result of these groundbreaking discoveries, there are now literally thousands of scientists studying novel forms of carbon and their properties.

The first fullerene to be discovered was C_{60}, with a structure described as similar to that of a football (soccer ball) [2] with pentagonal cycles separated by hexagonal ones, see Figure 1A. This so-called isolated pentagon rule (IPR) is thought to stabilize the fullerene structure, since pentagonal bonds cost more energy than hexagonal ones. The smallest fullerene is C_{20}, consisting of 12 pentagons. In general, a fullerene has n 3-valent vertices with 12 pentagons and $(n/2 - 10)$ hexagons, with $3/2n$ carbon-carbon bonds. Experimentally, C_{84} has been the largest fullerene [5] observed, but large 'carbon onions' [6] have been modeled theoretically. There are many isomers of the fullerene structures, so that several possible structures exist; however, most of these are not favored energetically.

Nanotubes were discovered in 1991 [3], as straight 'helical' coils of carbon, although filamentous carbon [7] was known prior to 1991. Thus a nanotube can be thought of as a rolled up sheet of graphene, with hemispheres of fullerenes at the ends. A commonly accepted growth mechanism [8,9] is that nanotubes form by catalytic action of transition metals, such as iron or cobalt, with a cap at one end and the open growth end eventually becoming closed after some aspect ratio is created. The nanotube analogue to C_{60}, the most common fullerene, seems to be a (10,10) nanotube capped with hemispheres of C_{240} [8], see Figure 1B and 1C.

Nanotubes are defined [10] by their 'chiral vector', or angle cut through the 2D layer of graphene, with

$$C_h = na_1 + ma_2 = (n, m) \tag{1}$$

where the indices (n, m) describe the number of unit vectors in the hexagonal graphene honeycomb lattice. There are two common geometries, a 'zigzag' nanotube, with a chiral angle of $\theta = 0°$, and an 'armchair' nanotube with $\theta = 30°$,

leaving a general chiral nanotube with $0 \leq \theta \leq 30^{\circ}$. The chiral angle is given by:

$$\theta = \tan^{-1}[\sqrt{3}m/(m+2n)] \tag{2}$$

and the nanotube diameter is

$$d_i = C_h/\pi = \sqrt{3}a_{c-c}(m^2+mn+n^2)^{1/2}/\pi \tag{3}$$

where a_{c-c} is the carbon – carbon nearest neighbor distance (1.421 Å) in graphite. Thus the (10,10) nanotube is of the armchair variety.

Graphene, or a 2D layer of graphite was originally [4] created by exfoliation, i.e., mechanical separation of the layers into few layers of graphene. This 2D form of carbon has exceptional [4] electronic properties. An experimental method of making finite graphene is by using catalytic metal nanoparticles [11] cutting along crystallographic planes. When restricting the 2D sheet character of graphene by one dimension, one creates graphene nanoribbons (GNRs), and with two-dimensional confinement, one creates GNFs, which theory predicts to have unique magnetic [12-14], optical [15], and spintronic [16] properties.

An interesting question to consider when thinking about the thermal character of GNFs, is whether they are actually stable, or would they transform to another form of carbon, such as the fullerene or CNT shapes? This question has been modeled by density functional theory (DFT) and *ab initio* molecular dynamics (MD) calculations, with the result [17,18] that GNFs do not transform to a different allotrope, but neither are they truly 2D, in the sense that the structure of the GNF becomes buckled and rippled at elevated temperatures. Annealing of the structures [17] found out-of-plane distortions as the temperature increased to 2400K, but no fundamental change in structure occurred.

In the laboratory, the progress in creating GNFs is behind that of theoretical modeling. GNFs have been created using a 'top-down' approach from exfoliation of graphite [19], to chemical vapor deposition [20,21], to arc-discharged material [22]. Among the properties examined, electron field emission has predominated [19,21]. To date, a true nanoengineering 'bottom-up' approach remains open to development, although some progress [23,24] has been made, especially for GNRs [25]. Thus, the truly exotic properties of GNFs remain to be explored.

Experimentally, one would like to place fullerenes, quantum dots, nanotubes, and GNFs in specific locations and ideally, ordered in a desirable location. The terms 'ordered' and 'highly ordered' frequently appear in the literature when authors describe the arrays they manufacture for nanoscale science and technology. We present a real space and a reciprocal space technique to give quantitative measure to these terms. The Fourier transform of the real space coordinates enables us to calculate an order parameter as a ratio of intensity to the full width half maximum σ of the FFTs. Defined as intensity I_r/σ_r, this parameter takes values from $[0, \approx 10]$ where larger values represent more order in the array.

A common method of array fabrication is that from anodized aluminum oxide [26-28]. In this method, a foil or thin film of aluminum is anodized in an acid to form porous aluminum oxide. To create an ordered array, frequently a two-step [29] procedure is used. The acid and voltage used determine the pore size and interpore distance [26]. The smallest pores are made using sulfuric acid while oxalic and phosphoric acid can be used to create larger pores. The porous array is then filled with the material of choice to create nanowires or nanotubes, or the oxide may be thinned to form a template for the placement of nanodots. The technique of imprint lithography [26,27] has also been used to form dimples on an aluminum surface as a guide to pore generation.

Order in arrays can result in physical properties not attainable from random or disordered arrays. Some examples include field emission from carbon nanotubes [30], magnetic arrays where the magnetism is affected by a demagnetization factor from neighboring magnetic nanowires [31], and in electronics, optoelectronics, sensing, high-density storage, and ultra-thin display devices [32]. Carbon nanotubes need to be spaced for field emission properties, so that the effects of screening are minimized. Arrays of nanotubes can be fabricated through the use of anodized aluminum oxide [33] and nanosphere lithographic techniques [34].

An order parameter has previously [35] been used to describe the order in fast Fourier transforms (FFTs) taken from nanoporous arrays. Denoted as (I/σ), it describes the ratio of the spot intensity I, and its full width at half-maximum (FWHM) σ of the FFT images taken from scanning electron micrographs. This parameter (I/σ) has been said [35] to be consistent with human recognition of the spatial order of holes. The order parameter (I/σ) takes values from $[0, \infty]$, and has been plotted [36] vs. several variables of pore formation. Typically, one looks for a maximum in the plot to determine the optimum conditions for ordered pore formation. We use FFTs generated from images that previously had no FFT data to determine the order in the arrays. We note that this type of analysis can be used in conjunction with any imaging device not having FFT capability.

Statistical parameters

We employ a graph-theoretical approach, where nodes represent atoms, and an edge represents a bond between sites, $G = (V, E)$. We create a graph of the nanosized form of carbon by creating bonds (links) between nearest neighbors up

N	N_1	N_2	N_3	N_C	Ave Bond Å
50	5	18	27	2.44	1.4248
100	7	26	67	2.60	1.4219
500	16	62	422	2.812	1.4228
1000	22	86	892	2.87	1.4229
2500	35	138	2327	2.9168	1.4239
5000	50	198	4752	2.9404	1.4238

Table 1: N is the number of atoms in the GNF, N_1, N_2, and N_3, are the number of one, two, and three fold coordinated atoms in the GNF, and N_C is the coordination number. The average bond length is in Angstroms.

to 1.3 times the shortest neighbor distance. These vary from 20 to 8000 atoms for fullerenes, nanotubes, and GNFs. An adjacency matrix is created and may exist in two forms. The standard form [37] is

$$A = \begin{cases} H(r_c - r_{ij}), & i \neq j \\ 0, & i = j. \end{cases} \tag{4}$$

where the Heaviside step function $H(r_c - r_{ij}) = 1$ if $r_c < 1.3*$(shortest distance to r_{ij}), and i and j represent atomic sites, and r_c is the cutoff value. Alternatively, we may consider the actual Euclidean distances in the adjacency matrix [38,39], so that $H(r_c - r_{ij}) = e_{ij}$, the Euclidean distance between atoms.

The approach to modeling the free energy, enthalpy, and entropy has been discussed in the literature [40,41]. These can all be determined from the appropriate adjacency matrix. We also calculate one of the oldest indices, the Wiener index [1], as

$$W = \frac{1}{2} \sum_{i=1}^{N} \sum_{j=1}^{N} d_{ij} \tag{5}$$

where N is the number of atoms and d_{ij} is the shortest path distance between atoms i and j. In the standard form, the distances between atoms = 1, and in the Euclidean form [38], it is e_{ij}, so that we calculate WE, the Euclidean 3D Wiener index. The collection of data starts from the atomic coordinates, and proceeds to calculating the adjacency matrix, and from it, all the results come from one MATLAB routine.

In Fig.1, we show plots of finite nanocarbons, $C_{60}(I_h)$, $C_{240}(5\nu)$, $a(10,10)$ nanotube and a rippled GNF with 500 atoms. In our notation, the fullerene isomers are listed in parentheses as Ih or 5ν. The fullerenes and nanotubes have atoms with 3 – fold coordination and the hexagonal and pentagonal cycles are shown in grayscale. For the GNFs the edge and corner atoms exist as shown in the figure, and the coordination is as tabulated for the 50-5000 atom structures in Table 1. The coordination number of the GNF, N_C, ranges from 2.44 to 2.9404. The bond length varies around 1.42 Å. A histogram of the various bond lengths in the 500-5000 atom GNFs is shown in Fig.2, and the bond lengths range from 1.33 Å to 1.52 Å.

Once we have created the adjacency matrix, the statistical mechanics data can be calculated [40,41]. The partition function is:

$$Z(G, \beta) = \mathrm{Tr}(e^{\beta A}) \tag{6}$$

where A is the adjacency matrix for the graph G, and $\beta = \mathrm{Tr}(e^{\beta A}) = 1/(k_B T)$. At $T = 300K$, we have β =38.68173/eV. The entropy can be determined as

$$S(G, \beta) = -k_B \sum_j \lambda_j p_j + k_B \ln(Z) \sum_j p_j \tag{7}$$

where λ_j is the eigenvalue of A and

$$p_j = \frac{e^{\beta \lambda_j}}{Z(G, \beta)} \tag{8}$$

is the probability that the ensemble occupies a microstate j. The free energy is the natural logarithm of the partition function,

$$F(G, \beta) = -\frac{\ln Z(G, \beta)}{\beta} \tag{9}$$

and the enthalpy can be defined as follows:

$$H(G, \beta) = -\frac{1}{Z(G, \beta)} \mathrm{Tr}(A e^{\beta A}). \tag{10}$$

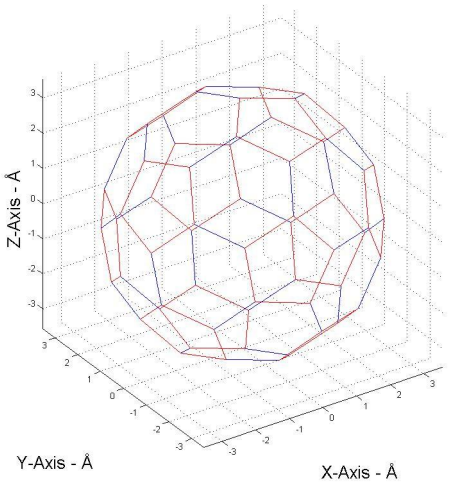

A. C_{60}. Grayscale indicates pentagonal cycles in the structure.

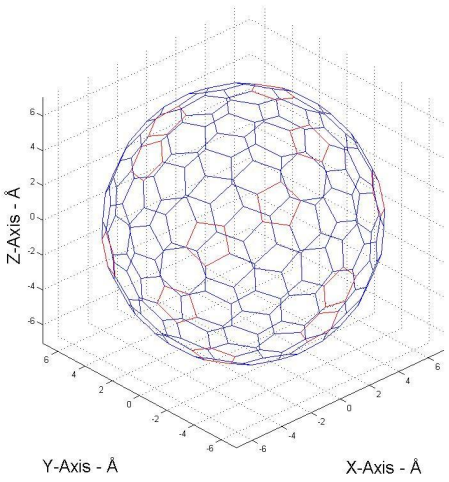

B. C_{240}. Grayscale indicates pentagonal cycles in the structure.

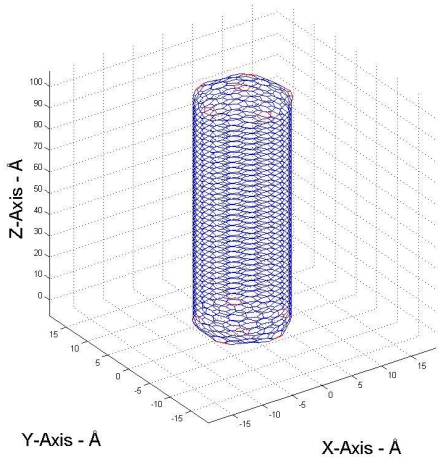

C. carbon nanotube (10,10) 100 Å

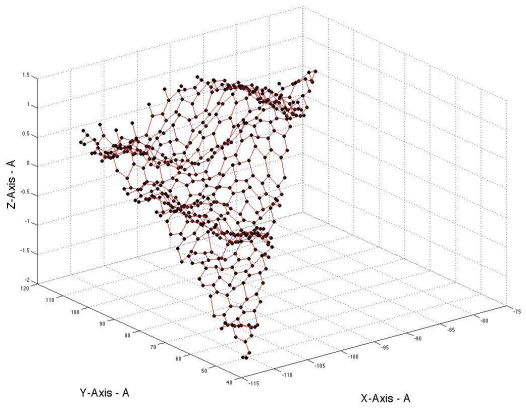

D. 3D rippled GNF with 500 atoms

Figure 1: MATLAB plots

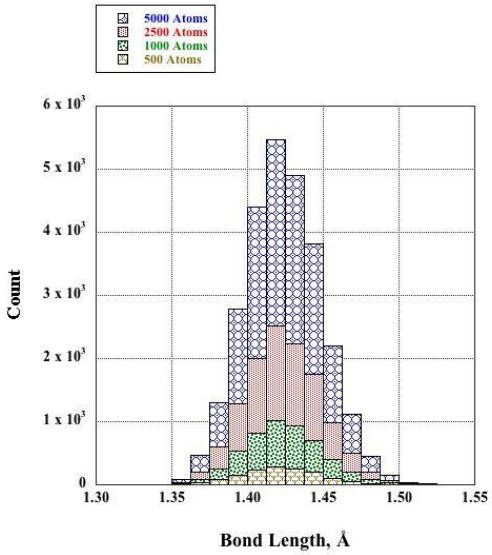

Figure 2: Histogram of the bond lengths (in Angstroms) of the 500-5000 GNFs.

We then plot the free energy, enthalpy, and entropy, per bond, versus the number of bonds in the nanocarbons. This results in plots with good power law [42] regression statistics as shown in Figs. 3 & 4. In Figure 3, we plot the data/bond versus the number of bonds for fullerenes and nanotubes. Figure 4 shows corresponding plots for GNFs. The distinction between (a) and (b) is that in (a), we have used an adjacency matrix with Euclidean distances, and in (b), we have used the standard adjacency matrix with zeros and ones. The best-fit equations in (a) have different leading coefficients, so that the entropy and enthalpy coincide (neglecting the sign difference) for small ($\approx$ 50 atoms) nanocarbons, and since the slope is different, the plots diverge for larger structures. Since we use a value of the Boltzmann constant in terms of eV, the values of our thermodynamic calculations for the GNFs with the state of $N_B = 1$ and $N = 2$ are: entropy, 1.1571 eV/K, enthalpy, 2.6296 eV, and free energy, 0.0807 eV. These quantities are divided by the number of bonds in the nanocarbon and plotted versus NB, to give a power law plot. The asymptote of zero for large N_B makes intuitive sense, since if we imagine the data/bond is finite, then as the number of bonds becomes large, we have zero as a limit. Note that the free energy and enthalpy have their signs reversed to allow them to be plotted.

For the fullerenes and nanotubes, we can calculate the energy of formation based on the types of bonds [43] in the structures, see Table 2. We use three types of bonds, as hh, hp, and pp, indicating hexagonal or pentagonal edges, and then further subdivided as to whether the opposite ends of the bond meets a hexagonal or pentagonal cycle. This gives a total of nine bonds and the heat of formation can be calculated as:

$$\delta H_f = \sum_{i}^{motifs} \varepsilon_i n_i \tag{11}$$

where ε_i is the energy contribution of each structural motif (nine) and n_i is the number of bonds associated with that motif. Since fullerenes have been analyzed extensively [43-45], we show ΔH_f versus length in Angstroms for two of the more common nanotubes, the (5,5) and (10,10) armchair varieties. For nanotubes, the heat of formation includes the energy to create the cap and then the length of the tube. We plot these results in Fig. 5. The (5,5) nanotubes contain a cap of C_{60} which has 60 ph_h^h bonds and 30 hh_p^p bonds to give $\Delta H_f = 654$ kcal/mol. As the length of the nanotube increases, we add hh_h^h bonds at 1.7 kcal/mol for each bond. The (10,10) nanotubes have a cap of C_{240} (see Fig 1B), which has 60 ph_h^h bonds, 60 hh_p^h bonds, and 240 hh_h^h bonds, to give $\delta H_f = 1158$ kcal/mol. Again, as the length of the nanotube increases, we add hh_h^h bonds at 1.7 kcal/mol for each bond. From the graph, we see that since the (10,10) tube is larger, the slope is 41.63 kcal/mol per Å length versus 20.689 kcal/mol per Å length for the (5,5) nanotube. For the (10,10) nanotubes, this gives a cap energy of 64 eV and a length energy of 1.8 eV/Å. These data are in good agreement [8] (40 eV and 0.74 eV/Å) with estimated measurements.

Since we are using a graph-theoretical language, we also calculate the Wiener index for fullerenes and nanotubes, based on the coordinate information in MATLAB. We note that for fullerenes, the Wiener index of $C_{60}(I_h) = 8340$ has been known since 1992 [47], and since then some additional results have been calculated [48-51]. The Weiner index for armchair and zigzag nanotubes has been known since 2004 [52,53]. In Table 3, we list some of the Wiener indices for the

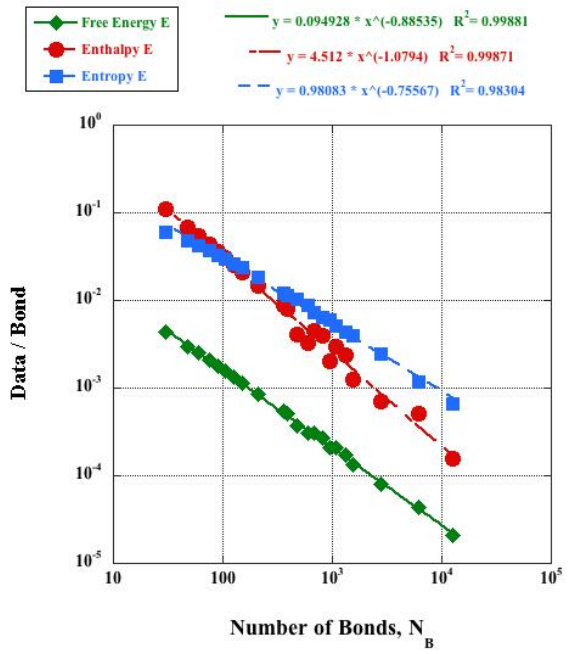

(a) Plots of the free energy, enthalpy, and entropy / bond versus the number of bonds. The data clearly exhibits power law character. This plot uses a Euclidean adjacency matrix.

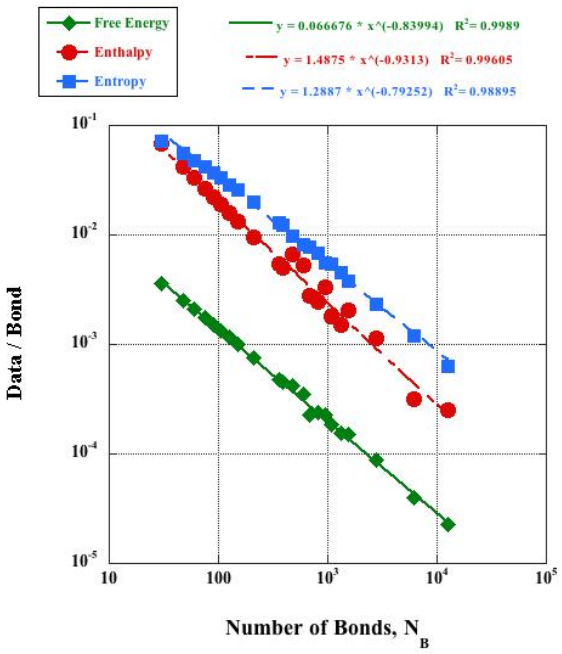

(b) Plots of the free energy, enthalpy, and entropy / bond versus the number of bonds. The data clearly exhibits power law character. This plot uses a standard adjacency matrix.

Figure 3: Power law plots for fullerenes and nanotubes.

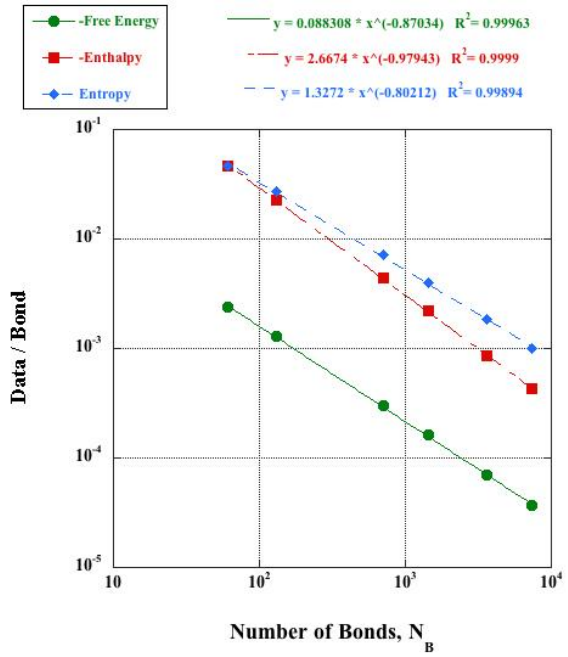

(c) Plots of the free energy, enthalpy, and entropy / bond versus the number of bonds. The data clearly exhibits power law character. This plot uses a Euclidean adjacency matrix.

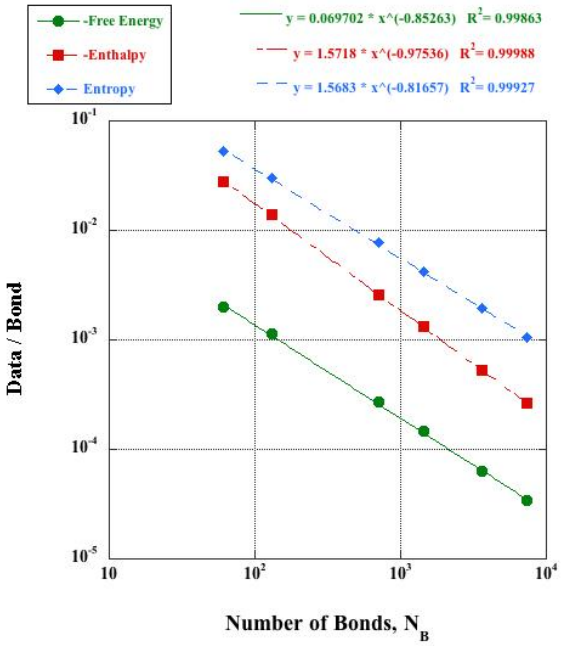

(d) Plots of the free energy, enthalpy, and entropy / bond versus the number of bonds. The data clearly exhibits power law character. This plot uses a standard adjacency matrix.

Figure 4: Power law plots for GNFs.

N	N_B	Nano-structure	Wiener Index (W)	Euclidean Wiener Index (WE) (W_E)	Ave Bond (Å)
20	30	$C_{20}(I_h)$	500	710.02423	1.4200
32	48	$C_{32}(D_{3d})$	1696	2408.3699	1.4200
40	60	$C_{40}(T_d)$	3000	4260.0679	1.4200
50	75	$C_{50}(D_3)$	5275	7490.6239	1.4200
60	90	$C_{60}(I_h)$	8340	11917.75156	1.4320
70	105	$C_{70}(D_{5h})$	12375	17672.68417	1.4307
84	126	$C_{84}(D_2)$	19646	28041.35179	1.4303
240	360	C_{240}	277440	392329.2316	1.4187
540	810	C_{540}	2119320	2994979.407	1.4190
720	1080	C_{720}	4352340	6162553.116	1.4207
100	150	(5,5)5	30580	42310.62308	1.3879
140	210	(5,5)10	72860	101743.2403	1.3962
260	390	(5,5)25	383700	541217.5044	1.4059
460	690	(5,5)50	1899100	2689448.448	1.4107
880	1320	(5,5)100	12350940	17526597.26	1.4150
4120	6180	(5,5)500	1186916820	1685572294.8	1.4164
320	480	(10,10) 5	569680	804021.9498	1.4156
400	600	(10,10) 10	997120	1410161.755	1.4165
640	960	(10,10) 25	3341840	4737709.644	1.4178
1040	1560	(10,10) 50	12327040	17496098.43	1.4193
1860	2790	(10,10) 100	62759375	89129458.54	1.4187
8360	12540	(10,10) 500	5046069000	7169083944.2	1.4199

Table 2: N is the number of atoms in the nano object, fullerenes are denoted by C_N, and nanotubes by their chiral indices followed by their length in Angstroms. The topological Wiener Index is W, and the Euclidean Wiener Index is W_E. The bond length is in Angstroms.

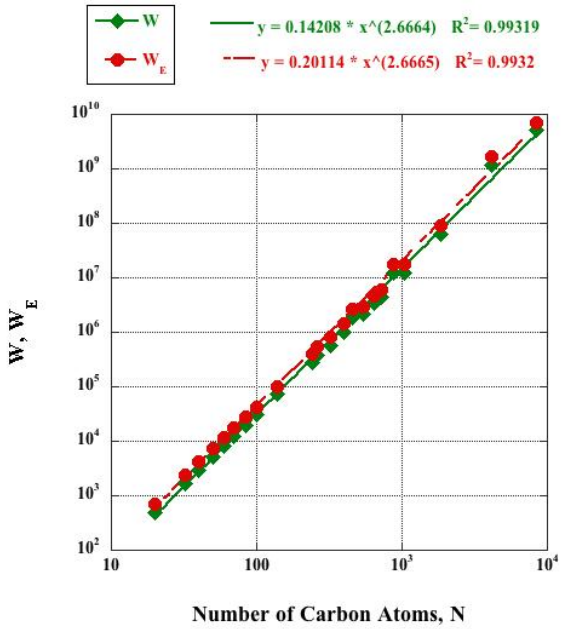

Figure 5: Heat of formation for (5,5) and (10,10) armchair nanotubes versus length in Angstroms.

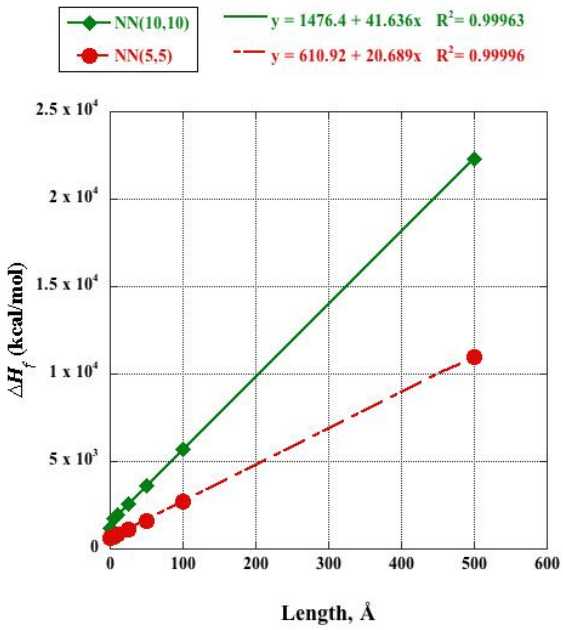

Figure 6: Power law plot of the Wiener Index (standard and Euclidean) for fullerenes and nanotubes versus the number of atoms, N.

fullerenes we investigate, and also the (5,5) and (10,10) nanotubes [54]. The Wiener Index for the fullerenes up to C84 agree with previous [48] results, and we add new results up to C_{720} and also the Euclidean indices for all nanocarbons. In Fig. 6, we plot the Wiener index versus N, the number of carbon atoms, to give a power law relationship. We note that for the fullerenes, the Wiener index depends on the structure, so each isomer has a different value for the index.

We now proceed to calculate some related parameters of interest for GNFs. In the harmonic approximation [55], the frequency of the stretching vibration of a carbon-carbon bond is given by:

$$\nu = \frac{1}{2\pi}\sqrt{\frac{k}{\mu}} \tag{12}$$

where k is the force constant (about 305 N/m for graphene [56] between nearest neighbor carbon atoms and μ is the reduced mass. The total intramolecular energy, E_{int} can be divided into two parts; a variable term U_{var} and a constant

Structural Motif	ε_i.(kcal/mol)
pp_p^p	19.8
pp_p^h	17.6
pp_h^h	10.3
ph_p^p	15.7
ph_p^h	12.4
ph_h^h	7.8
hh_p^p	6.2
hh_p^h	4.7
hh_h^h	1.7

Table 3: Heat of formation parameters for the nine structural motifs.

term U_{con}. We conclude that the variable term can be written [55] as:

$$U \cong \sum \frac{1}{\sqrt{M_1 M_2 / M}} \tag{13}$$

where the proportionality constant depends on the force constant, but not the mass dependence. If we rewrite this in terms of our GNF, we have:

$$\sum \sqrt{\frac{n}{C n_1 n_2}} \tag{14}$$

where $n = n_1 + n_2$, and n_1 and n_2 are the number of carbon atoms on the two sides of the vibrating bond. We may compare this to the relationship [1,55] for the Wiener index:

$$W = \sum n_1 n_2 \tag{15}$$

Now in order to linearize U, we note that the minimum and maximum values of the product $n_1 n_2$ are $(n-1)$ and $(n/2)^2$, respectively. The middle value is

$$\xi = \frac{n^2}{8} + \frac{n-1}{2} \tag{16}$$

and we expand U as a power function about $x = \xi$

$$(Cx)^{-1/2} \approx f(\xi) + f'(\xi)(x - \xi) \tag{17}$$

where

$$f(\xi) = \frac{1}{\sqrt{C}} \sqrt{\frac{8n}{n^2 + 4n - 4}} \tag{18}$$

If we write $C = 12$ amu, then to a first approximation we have

$$U \approx \frac{1}{\sqrt{12}} N_B \sqrt{\frac{8n}{n^2 + 4n - 4}} \tag{19}$$

Since n is the number of atoms in the GNF and we calculate N_B through each iteration of the MATLAB program, we can determine the approximate values for U. Now both U and W have power law character, so we plot U versus W and W_E in Figure 7. These results show good regression features. The only distinction is that W_E has slightly larger values (W multiplied by the bond length), but behaves in the same manner as W.

In the harmonic approximation, we may also consider the vibrational excitation energy from the static position of the GNF. Previous calculations [36], show that the summed displacement may be calculated as:

$$\langle X_i X_i \rangle = \sqrt{\sum_{i=1}^{n} (\Delta x_i)^2} = \sqrt{\frac{W}{nk\beta}} \tag{20}$$

where $\beta = 38.68173$/eV, k is the force constant between carbon atoms (305 N/m), n is the number of atoms, and W is the Wiener index. In Fig. 8, we show the dependence of N_B, U, W, and $\langle XX \rangle$ on the number of carbon atoms N. The values of the summed displacement range from 0.4760 Å to 14.7106 Å for 50 to 5000 atoms, respectively. If we were to consider the average displacement per bond, the values would be 0.0039 Å and 0.000747 Å, for 50 and 5000 atoms, respectively. The data all show good regression features.

Nanoporous arrays

Nanoporous arrays are useful for defining a regular arrangement of pore size and geometry. The pore can then be filled with nanosized objects such as quantum dots, fullerenes, nanotubes, or GNFs. Typically, the properties of nanosized material depend on the exact size and amount of order in the array, so that precise control of the patterns are desirable. Three types of geometry of pore arrangements are common: hexagonal, triangular, and square.

The Archimedean lattices describe methods of tiling the plane with geometric polygons [57]. For these, we require: (a) that the tiling be edge-to-edge; (b) that the tilings be regular polygons; and (c) that all vertices be of the same type [58]. This then results in 11 distinct tilings known as the Archimedean or Kepler tilings. The Schläfli symbols that describe the polygon type and the degeneracy type that meets at an equivalent vertex labels them appropriately. If we further require

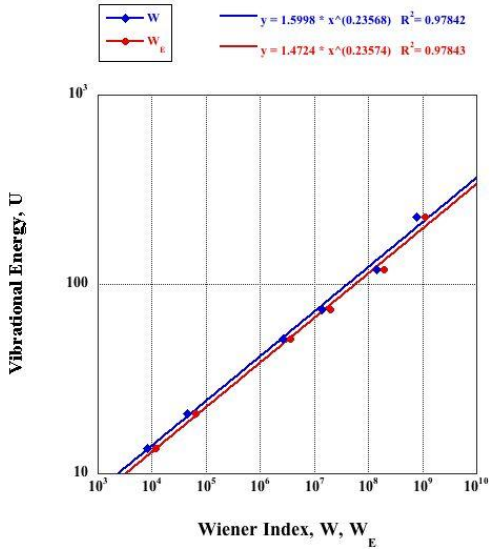

Figure 7: Vibrational energy, U, versus the standard Wiener index, W, and the 3D Euclidean Wiener index W_E. The data follows a power law.

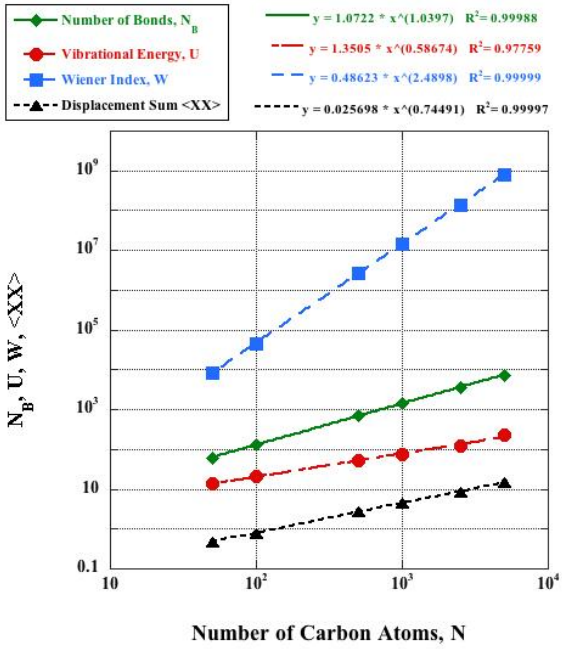

Figure 8: Power law plots of N_B, U, W, and $\langle XX \rangle$ versus the number of carbon atoms, N. The statistics and regression of the data are quite good.

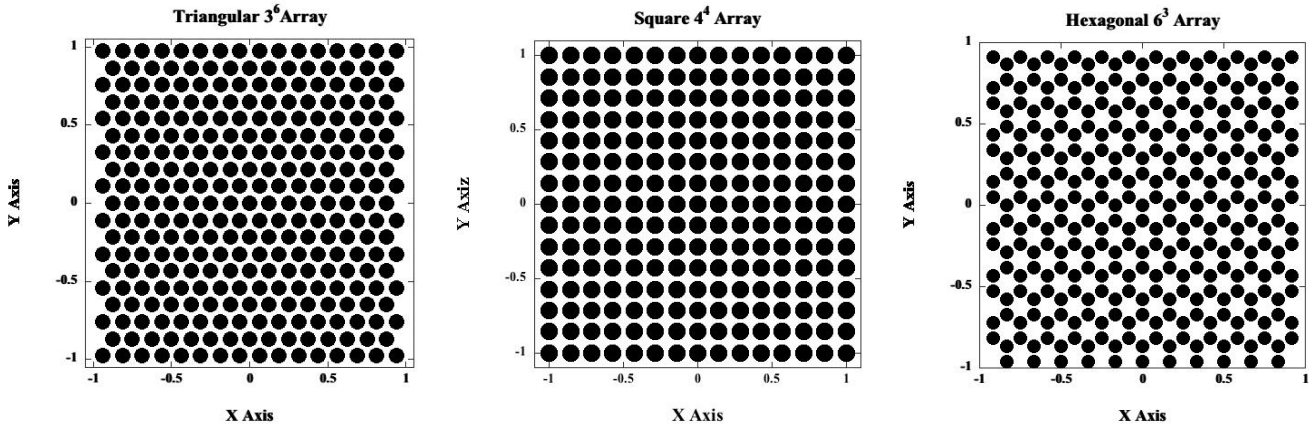

A: triangle 3^6 B: square 4^4 C: hexagonal 6^3

Figure 9: Mathematically ordered porous arrays

that the tilings be constructed with regular polygons that are monohedral, i.e., the same size and shape, we have the three regular tilings, 3^6, 4^4, and 6^3. Examples of these as porous arrays are shown in Fig. 9.

If we consider that the regular tilings constitute an array, with lattice points resulting in a pore, then these regular tilings have all been fabricated into ordered arrays by lithographic means [59]. Ordered porous arrays normally have triangular symmetry due to dense close pack spacing of the pores. For other applications of ordered arrays, the reader is directed to the review in reference [60].

The regular tilings can be generated by the equations:

$$a_1 = a\hat{x}, \quad a_2 = a\cos(\frac{2\pi}{n})\hat{x} + a\sin(\frac{2\pi}{n})\hat{y} \tag{21}$$

where a_1 and a_2 are basis vectors for the sites or pores, a is the distance between lattice points, n is the symmetry of the lattice, 3, 4, or 6, and $\hat{x}$m $\hat{y}$^ are unit vectors in the x and y directions. In addition, a hexagonal tiling is actually constructed from two interconnected equilateral triangles with a basis shift of the second triangle given by:

$$b_x = a_{1x} + a_{2x} + a \cdot \frac{1}{2}, \quad b_y = a_{2y} + a \cdot \frac{\sqrt{3}}{6} \tag{22}$$

where a is again the distance between sites. Alternatively, one may use the hexagonal basis set [9], where the vectors:

$$a_1 = \left(\frac{\sqrt{3}}{2}a, \frac{a}{2}\right), \quad a_2 = \left(\frac{\sqrt{3}}{2}a, -\frac{a}{2}\right) \tag{23}$$

generate the hexagonal lattice and a is the lattice constant of the 2D network.

The order parameters we use have been introduced in previous publications on ordered arrays [61], and in image analysis of bee honeycomb as porous arrays [62]. Suppose there are N_T total cells (about 200 in a typical image), and N centers from which the radial distribution function (RDF) and PDF are calculated ($N = 19$ in our examples, 13 for the square array), and let r_{ij} be the distance between the centers of cell i and cell j. To make the analysis scale independent, we use the average distance a of two neighboring cells as a unit and in the rest of this chapter we shall assume that this rescaling has been done. This a is called the lattice constant of the array. Then, the RDF is defined [63] by

$$R(r) = \frac{1}{N}\sum_{i=1}^{N_T}\sum_{j=1}^{N_T}\delta(r - r_{ij}) \tag{24}$$

where the $\delta(r)$ is a delta function. N is less than N_T to minimize edge effects in the calculated PDF and RDF, for a center near the edge would have only three or fewer neighbors. The N centers should be chosen near the center of the image. There will be a peak around 1, the average distance between two neighboring cells, another peak around the average distance between the center of a cell and the centers of the next-to-closest ones. The PDF is then obtained by:

$$\rho(r) = \frac{1}{2\pi r}R(r) \tag{25}$$

Nearest Neighbor	1	2	3	4	5	6	7	8	9
Triangle r/r_0	1	$\sqrt{3}$	2	$\sqrt{7}$	3	$\sqrt{12}$	$\sqrt{15}$	4	
N_C Triangle	6	6	6	12	6	6	12	6	
Hexagion r/r_0	1	$\sqrt{3}$	2	$\sqrt{7}$	3	$\sqrt{12}$	$\sqrt{15}$	4	
N_C Hexagon	3	6	3	6	6	12	3	6	
Square r/r_0	1	$\sqrt{2}$	2	$\sqrt{5}$	$\sqrt{8}$	3	$\sqrt{10}$	$\sqrt{13}$	4
N_C Square	4	4	4	8	4	4	8	8	4

Table 4: Nearest neighbor values for the three regular tilings and the values of N_C.

where $\rho(r)$ is the PDF. The coordination number of a peak is derived from the RDF is:

$$N_C = \sum_{i=r_1}^{r_2} R(r_i) \tag{26}$$

where $R(r)$ is the RDF, NC is the coordination number of a nearest neighbor site, and r_1 and r_2 define the limits of the peak in the RDF. For the arrays we examine, $N_C = 4$ for the first peak of the square array, $N_C = 6$ for the first peak of the triangular array, and $N_C = 3$ for the first peak of the hexagonal array.

Now $R(r)$ as we have defined it (and hence also $\rho(r)$) is only non-zero in a finite number of r-values, which can also conveniently be represented by a bin diagram. Suppose the bin size is 0.02 and that we consider 205 bins, which is enough to include the first 8 or 9 peaks, and includes some extra to get the right side of the last peak. We then define a disorder parameter as:

$$\Delta\Phi = (0.02) \sum_{\xi=0.02}^{4.1} \rho(r_\xi) - (0.06) \sum_{\xi=n(r_\xi)} \rho(r_\xi) \tag{27}$$

Note that this disorder parameter is simply the sum of the product of the width of the bins (0.02) multiplied by the height of the PDF (the amount in the bin) and subtracting the amount in an ideal location. For very narrow bins these sums are integrals. Therefore, if all the contribution comes from the PDF in the ideal state $\Delta\Phi = 0$. In general, ξ is stepped by the bin width, 0.02. In the sum of the subtracted term, $\xi = n(r_\xi)$, the ideal eight or nine scaled nearest neighbors positions, and includes a bin above and below the (rounded) nearest neighbor location. The subtracted term is the amount in an ideal location and it is distributed over three bins. Three bins are used since our modeling shows that it is difficult to generate a PDF of an ordered array with $\Delta\Phi = 0$ in a computer model unless one takes a bin above and below the nearest neighbor locations, $n(r_\xi)$, some of which are irrational, see Table 4. This results in a rather sensitive order parameter

$$\Phi = 1 - \frac{\Delta\Phi}{(0.02)\sum_{\xi=0.02}^{4.1} \rho(r_\xi)} \tag{28}$$

where Φ takes values from $[0, 1]$ and equals one when there is no disorder.

We create a reciprocal space order parameter from the FFT of the real space data. The intensity, I, is determined from a Fourier transform of the data:

$$\begin{aligned} &I(k_x, k_y) = |F|^2 \\ &F = X(k_x, k_y) = \sum_{n_1=0}^{N_1-1} \sum_{n_2=0}^{N_2-1} x(n_1, n_2) W_{N_1}^{k_x n_1} W_{N_2}^{k_y n_2} \\ &\text{where} \\ &k_x = 0, 1, \ldots, N_1 - 1; \quad k_y = 0, 1, \ldots, N_2 - 1 \\ &W_{N_1}^{k_x n_1} = \exp(-2\pi i k_x n_1 / N_1); \quad W_{N_2}^{k_y n_2} = \exp(-2\pi i k_y n_2 / N_2) \end{aligned} \tag{29}$$

where $x(n_1, n-2)$ are the coordinates of the real space data, and F is the 2D discrete Fourier transform. The 2D FFT is determined using MATLAB, which uses the FFTW3 routine [64]. The FFT as determined by MATLAB, is sensitive to pore position and number of pore sites. We use array coordinates (about 250) normalized so that the largest distance is 1 unit, and the FFT has reciprocal units in K space from -10 to $+10$. If the FFT of the image is $Y = \text{fft2}(X)$, then

Array	Φ	I_r/σ_r
Hexagon 3^6	1.00	6.71
Square 4^4	1.00	10.75
Triangle 6^3	1.00	5.39
Masuda 3^6	0.23	0.95
Masuda 4^4	0.20	1.65
Masuda 6^3	0.26	1.97

Table 5: Order parameters for the ideal arrays and for the lithographically defined arrays from reference [58].

this returns the two-dimensional discrete Fourier transform (DFT) of X, computed with a fast Fourier transform (FFT) algorithm, without zero padding. The resulting Y is the same size as X.

The order parameter generated from this data is defined as:

$$I_r/\sigma_r = \frac{I_1/I_0}{\sigma_1/\sigma_0} \tag{30}$$

where I_r is the relative intensity of the first order peaks with respect to the zeroth order peak, and σ is the FWHM (full width half maximum) of the first order peak next to the primary one. Note that others [35] have used a related order parameter. To model the FFT we use a sum of up to eight Gaussians:

$$I(K) = \sum_{i=1}^{8} a_i \exp\left(\frac{-(K-b_i)^2}{c_i^2}\right) \tag{31}$$

where a_i, b_i, and c_i are constants determined by the fit. The Gaussians are determined by the use of the Curve Fitting Toolbox (available as part of MATLAB).

In Figure 10, we show the results of using Excel macros to determine the RDFs and PDFs of the three regular arrays. Note that in the RDFs, the value of N_C is as shown from Table 1, with the caveat that some of the peaks are lowered due to their distribution over two bins. Also plotted are the RDFs and PDFs of the lithographically defined arrays as reported in reference [59]. For the mathematically determined arrays in Figure 1, the order parameter, Φ, has values of 1.0 (exactly) for each array, 3^6, 4^4, and 6^3. For the arrays in ref [46], the values of Φ are 0.26, 0.20, and 0.23, respectively for the triangular, square and hexagonal arrays. These values are summarized in Table 5.

For the order parameter determined by the FFT, we obtain values of I_r/σ_r of 6.71, 10.75, and 5.39 for the ideal ordered arrays 3^6, 4^4, and 6^3. The plots of the intensity versus K space are shown in Figure 11. We have artificially raised the curves for clarity. The order parameter is determined by the Gaussian curve fits, i.e., the values of $a(I)$ and $c(\sigma)$ in the fit to the FFT. In the MATLAB code we are able to determine the intensity in the center of the diffraction pattern along a line cut of zero degrees in reciprocal space. Note that since we are using an FFT of the real space coordinates, we have maximized the size of the pores so that the peaks in reciprocal space are as sharp as possible. This allows us to determine the maximum values of the order parameter. In comparison, the lithographically defined arrays from Ref [59], have $I - r/\sigma_r = 0.95$, 1.69, and 1.97 for the three cases of ordered arrays of 3^6, 4^4, and 6^3, respectively. In both the real space and reciprocal space order parameters, the experimental results are considerably less than the ideal values.

Conclusion

In summary, we have determined the power law behavior of the free energy, enthalpy, entropy, and atomic displacement of nanocarbons consisting of 20-8000 atoms. We use atomic coordinates to calculate the Wiener index for fullerenes, nanotubes, and GNFs. The vibrational energy versus the Wiener index shows power law character as well. There are some minor distinctions when using the Euclidean Wiener index, which we have included for completeness. The heat of formation of nanotubes follows a linear relationship with length in agreement with known data.

We also gave a quantitative analysis for porous arrays. Both real space and reciprocal space analysis has been done. The measured differences in the order parameters originate from the alternate ways they are defined. The order parameter Φ is a real space measure, essentially related to the height and width of the PDF histograms, while I_r/σ_r is related to its reciprocal space definition. Since the length scale is normalized, the methods described can be applied to any image

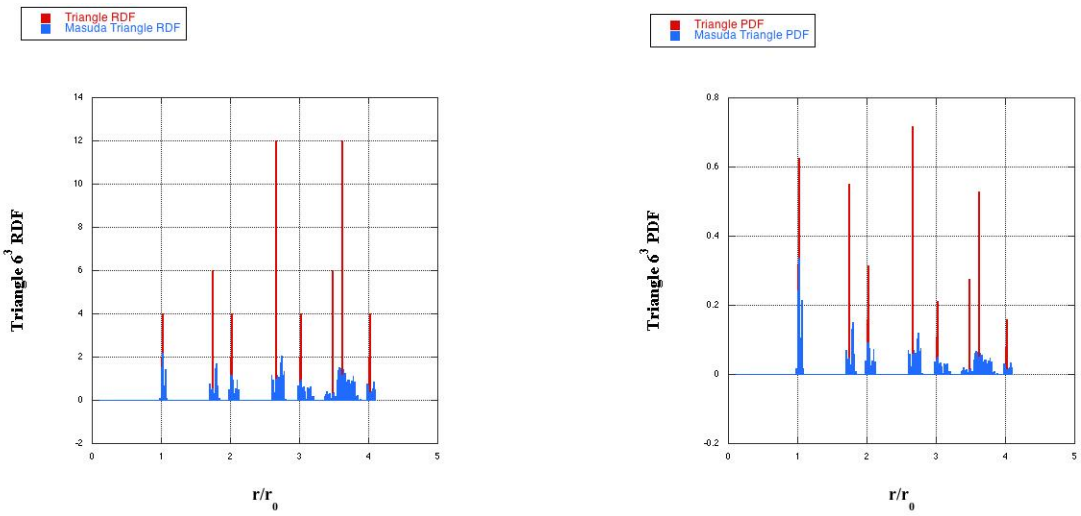

A. Triangle

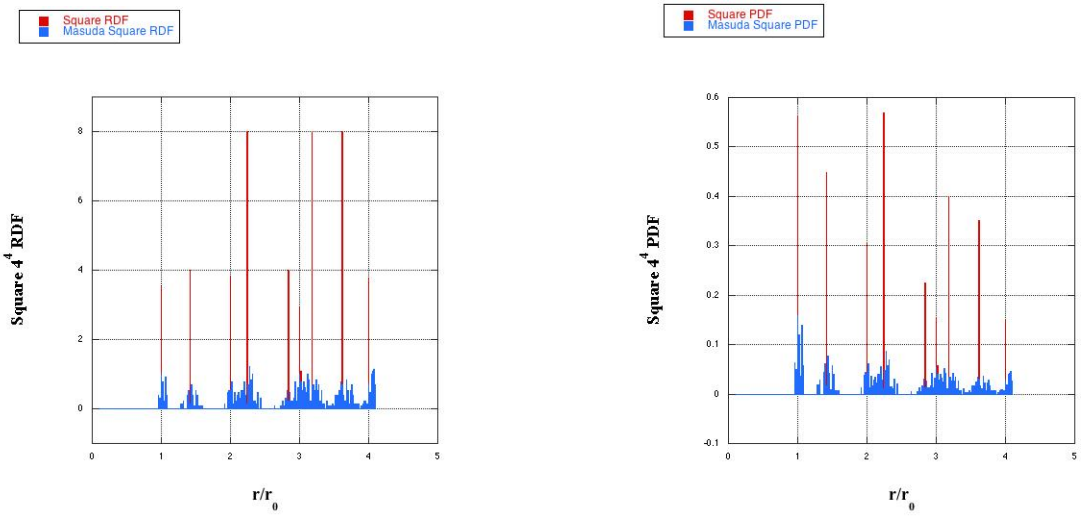

B. Square

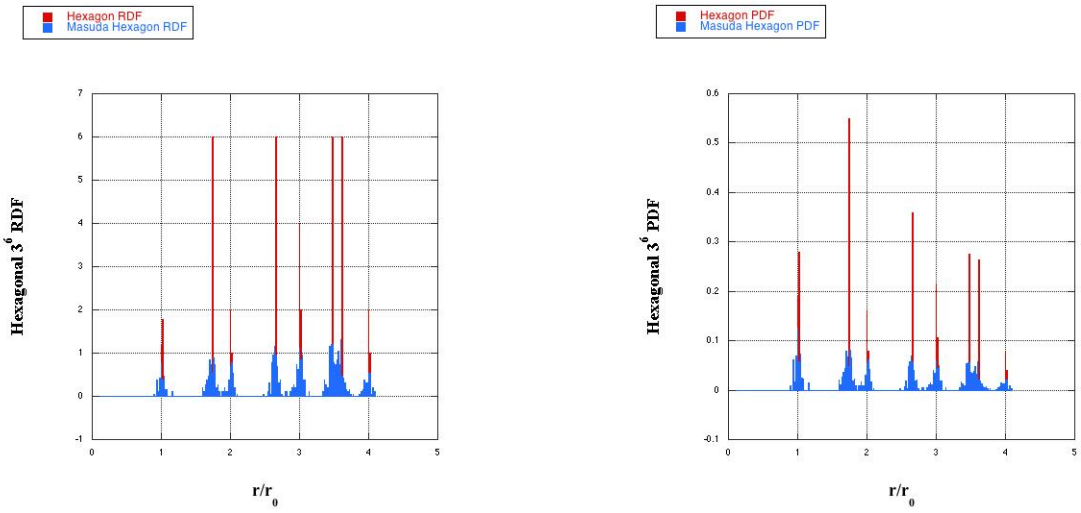

C. Hexagon

Figure 10: RDFs and PDFs of the ideal arrays with the results from Ref [3] superimposed

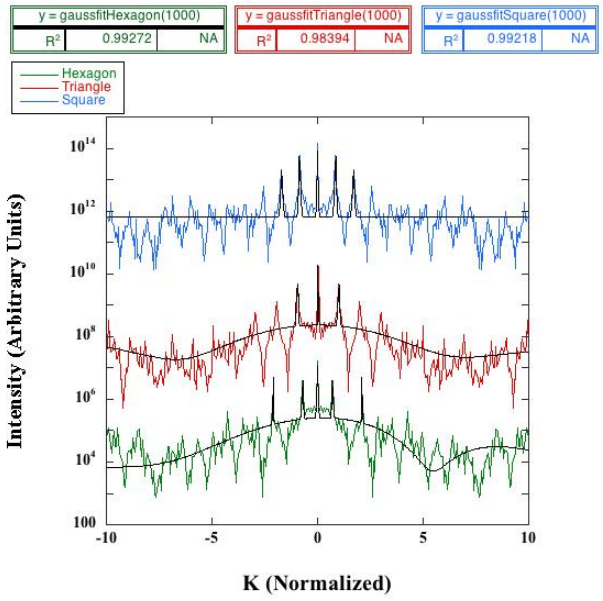

Figure 11: FFTs of the ideal arrays with Gaussian curve fits to the data. There is an artificial vertical shift to clarify the results.

and a corresponding order parameter can be calculated. The use of procedures applicable to general image analysis has determined order parameters for real space images and these methods are useful for determining the order in any porous array. The methods described in this chapter make use of widely available software to analyze porous arrays.

We have outlined procedures applicable to modeling finite nano systems using only the 2D or 3D coordinates of the structures. These methods will allow others to investigate similar types of models and we encourage the understanding of nano-geometries as we move into the 21st century.

Acknowledgements

F.H. Kaatz thanks A. Fasolino for sharing atomic coordinates of rippled graphene, and his collaborators for their insight and assistance with this project.

References

[1] H. Wiener, J. Am. Chem. Soc. 69, (1947) 17.
[2] H.W. Kroto, J.R. Heath, S.C. O'Brien, R.F. Curl, and R.E. Smalley, Nature 318 (1985) 162.
[3] S. Iijima, Nature (London) 354, (1991) 56.
[4] K.S. Novoselov, A.K. Geim, S.V. Morozov, D. Jiang, Y. Zhang, S.V. Dubonos, I.V. Grigorieva, and A.A. Firsov, Science 306, (2004) 666.
[5] T.M. Halasinshi, R. Ruiterkamp, F. Salama, B.H. Foing, and P. Ehrenfreund, Fullerenes, Nanotubes and Carbon Nanostructures, 19(5), (2011) 398
[6] Y.L Lin and F. Nori, Phys. Rev B 49(7), (1994) 5020.
[7] R.T.K. Baker, Carbon 27, (1989) 315.
[8] A. Thess, et al, Science 273 (1996) 483.
[9] C. Jin, K. Suenaga, and S. Iijima, ACS Nano, 2(6) (2008) 1275.
[10] M.S. Dresselhaus and P.C. Eklund, Adv. Phys. 49(6) (2000) 705.
[11] L. C. Campos, V. R. Manfrinato, J. D. Sanchez-Yamagishi, J. Kong, and P. Jarillo-Herrero, Nano Lett. 9(7), (2009) 2600.
[12] J. Zhou, Q. Wang, Q. Sun, and P. Jena, Phys. Rev. B 84, (2011) 081402.
[13] X. Li and Q. Wang, Phys. Chem. Chem. Phys. 14, (2012), 2065.
[14] W. Sheng, Z. Y. Ning, Z. Q. Yang, and H. Guo, Nanotechnology 21, (2010) 385201.

[15] A.M Silva, M.S. Pires, V.N. Freire, E.L. Albuquerque, D.L. Azevedo, and E.W.S. Caetano J. Phys. Chem. 114, (2010) 17472.
[16] W.L. Wang, O.V. Yazyev, S. Meng, and E. Kaxiras, Phys. Rev. Lett. (2009) 157201.
[17] H. Shi, A.S. Barnard, and I.K. Snook, Nanotechnology 23, (2012) 065707.
[18] A.S. Barnard and I.K. Snook, J. Chem. Phys. 128, (2008) 094707.
[19] S. Vadukumpully, J. Paul, and S. Valiyaveettil, Carbon 47, (2009) 3288.
[20] N. G. Shang, P. Papakonstantinou, M. McMullan, M. Chu, A. Stamboulis, A. Potenza, S. S. Dhesi, and H. Marchetto, Adv. Funct. Mater. 18, (2008) 3506.
[21] N. Soin, S.S. Roy, S. Roy, K.S. Hazra, D.S. Misra, T.H. Lim, C.J. Hetherington, and J. A. McLaughlin, J. Phys. Chem. 115, (2011) 5366.
[22] C.G. Salzmann, V. Nicolosi, and M.L.H. Green, J. Mater. Chem. 20, (2010) 314. [23] L. Zhi and K. Mullen, J. Mater. Chem. 18, (2008) 1472.
[24] F. Mercuri, M. Baldoni, and A. Sgamellotti, Nanoscale 4, (2012). 369.
[25] J. Cai, P. Ruffieux, R. Jaafar, M. Bieri, T. Braun, S. Blankenburg, M. Muoth, A. P. Seitsonen, M. Saleh, X. Feng, K. Mullen and R. Fasel, Nature 466, (2010) 470.
[26] Choi, J., Luo, Y., Wehrspohn, R.B., Hillebrand, R.B., Schilling, J. and Gösele, U. (2003) J. Appl. Phy. 94(8), 4757-4762.
[27] Asoh, H., Nishio, K., Nakao, M., Tamamura, T., and Masuda, H. (2001) J. Electrochem. Soc. 148(4), B152-B156.
[28] Li, A.P., Müller, F., Birner, A., Nielsch, K., and Gösele, U. (1998) J Appl. Phys. 84, 6023- 6026.
[29] Masuda, H. and Fukuda, K. (1995) Science 238, 1466-1468.
[30] Shang, X.F., Wang, M., Qu, S.X., Zhao, R., Zhou, J.J., Xu, X.B., Tan, M.Q., and Li, Z.H. (2008) Nanotechnology 19, 065708.
[31] Sellmyer, D.J., Zheng, M., and Skomski, R. (2001) J Phys Condens Matter 13, R433.
[32] Lei, Y., Cai, W., and Wilde, G. (2007) Progress in Materials Science 52, 465–539.
[33] Li, J., Papadopoulos, C., Xu, J.M., and Moskovits, M., Appl. Phys. Lett. 75, (1999) 367.
[34] Hulteen, J.C., Treichel, D.A., Smith, M.T. Duval, M.L., Jensen, T.R., and Van Duyne, R.P. (1999) J. Phys. Chem. B 103, 3854-3863.
[35] Shingubara, S., Okino, O., Sayama, Y., Sakaue, H., and Takahagi, T. (1997) Jpn. J. Appl. Phys. 36, 7791-7795.
[36] Rao YL, Anandan V, Zhang G (2005) J. Nanosci. Nanotechnol. 5:2070
[37] E. Estrada and N. Hatano. Chem. Phys. Lett. 486, (2010) 166.
[38] S. Nikolic, N. Trinajstic, Z. Mihalic, and S. Carter, Chem. Phys. Lett. 179, (1991) 21.
[39] A. Vodopivec, F.H. Kaatz, and B. Mohar, J. Math. Chem. 47, (2010) 1145.
[40] E. Estrada, and N. Hatano, Chem. Phys. Lett. 439, (2007) 247.
[41] F.H. Kaatz, E. Estrada, A. Bultheel, and N. Sharrock, Physica A 391 (2012), 2957.
[42] A. Clauset, C.R. Shalizi, and M.E.J. Newman, SIAM Rev. 51, 661 (2009).
[43] M. Alcami, G. Sanchez, S. Diaz-Tendero, Y. Wang, and F. Martin, J. Nanosci. Nantechnol. 7 (2007) 1329.
[44] A.A. Levchenko, A.I. Kolesnikov, O. Trofymluk, and A. Navrotsky, Carbon, 49 (2011) 949.
[45] A. Rojas, M. Marinez, P. Amador, and L.A. Torres, J. Phys. Chem. B 111 (2007) 9031.
[46] J. Cioslowski, N. Rao, and D. Moncrieff, J. Am. Chem. Soc. 122, (2000) 8265.
[47] O. Ori and M. D'Mello, Chem. Phys. Lett. 197 (1992) 49.
[48] K. Balasubramanian, J. Phys. Chem. 99 (1995) 10785.
[49] D. Babic, D.J. Klein, I. Lukovits, S. Nikolic, N. Trinajstic, Internat. J. Quantum Chem. 90, (2002) 166.
[50] P.W. Fowler, Croatica Chem. Acta 75(2), (2002) 401.
[51] H.R. Khataee, M.Y. Ibrahim, S. Sourchi, L. Eskandari, and M.A. Teh Noranis, COMPEL, 31(2) (2012) 387.
[52] P.E. John and M.V. Diudea, Croatica Chem. Acta 77(1-2) (2004) 127.
[53] M.V. Diudea, M Stefu, B. Parv, and P.E. John, Croatica Chem. Acta 77(1-2), (2004) 111.
[54] L.H. Gan and J.Q. Zhao, Physica E 41 (2009) 1249.
[55] I. Gutman and I.G. Zenkevich, Z. Naturforsch. 57, (2002) 824.
[56] S.Y. Davydov, Phys. of the Solid State 52, (2010), 1947.
[57] Grünbaum B and Shepard GC (1989) Tilings and patterns: an introduction. W.H. Freeman and Co., New York, NY
[58] De Graef M and McHenry ME (2008) Structure of materials. Cambridge University Press, Cambridge, UK
[59] Masuda H, Asoh H, Watanabe M, Nishio K, Nakao M, and Tamamura T (2001) Adv Mater 13:189
[60] Lei Y, Cai W, Wilde G (2007) Prog Mater Sci 52:465
[61] Kaatz, FH, Bultheel A, Egami T (2009) J Mater Sci. 44:40
[62] Kaatz FH, Bultheel A, Egami T (2008) Naturwissenschaften 95:1033
[63] Egami T, Billinge SJL (2003) Underneath the Bragg peaks: structural analysis of complex materials. Pergamon, Amsterdam

[64] Frigo, M and Johnson, SG (2005) Proc. IEEE: 93(2), 216